

# Autonomous Surface Vehicle Multistep Look-Ahead Measurement Location Planning for Optimal Localization of Underwater Acoustic Transponders

JESSE R. GARCIA , Student Member, IEEE  
JAY A. FARRELL , Fellow, IEEE  
ZAHER M. KASSAS , Senior Member, IEEE  
University of California, Riverside, CA, USA

MICHAEL T. OUMET  
SPAWAR Systems Center Pacific, San Diego, CA, USA

**An underwater vehicle may utilize underwater transponders (UTs) for navigation in the absence of global navigation satellite system signals. However, the position of each UT must be known by the underwater vehicle. The problem of an autonomous surface vehicle (ASV) optimally planning measurement locations to localize a set of arbitrarily predeployed acoustic UTs is considered. The ASV is assumed to make noisy range measurements to the UTs. A maximum *a posteriori* estimator is derived to localize the UTs. In addition, a multistep look-ahead (MSLA) ASV optimal measurement location planning (OMLP) strategy is developed. This planning strategy prescribes future multistep measurement locations. A physical interpretation of the proposed planner in the single-step, single transponder case is provided. Simulation results are presented demonstrating the tradeoff between expected localization performance and computational time associated with various look-ahead horizons and travel distances. Experimental results are given illustrating the proposed MSLA OMLP**

Manuscript received August 3, 2018; revised December 26, 2018; released for publication December 28, 2018. Date of publication April 4, 2019; date of current version December 5, 2019.

DOI. No. 10.1109/TAES.2019.2909253

Refereeing of this contribution was handled by Z. Davis.

This work was supported in part by the Office of Naval Research under Grant N00014-16-1-2768.

Authors' addresses: J. R. Garcia, J. A. Farrell, and Z. M. Kassas are with the Department of Electrical and Computer Engineering, University of California, Riverside, Riverside, CA 92521 USA, E-mail: (jegarcia@ece.ucr.edu; farrell@ece.ucr.edu; zkassas@ieee.org); M. T. Oumet is with the SPAWAR Systems Center, Pacific, San Diego, CA 92152 USA, E-mail: (ouimet@spawar.navy.mil). (*Corresponding author: Zaher M. Kassas.*)

0018-9251 © 2019 IEEE

strategy's performance in environments containing one and two UTs. The proposed OMLP strategy is able to localize UTs to within 4 m of their true locations. Additionally, increasing the planning horizon is demonstrated to yield better UT localization at the cost of increased computational burden.

## I. INTRODUCTION

Underwater vehicles require knowledge of their position to perform their mission [1]. Global navigation satellite system (GNSS) signals become severely attenuated underwater, rendering them unusable at depths below a few feet. Resurfacing to re-establish GNSS connection [2], [3] is not desirable in situations where stealth and covertness are required. The underwater vehicle may instead rely on signals from underwater transponders (UTs) with known locations to determine its position estimate. This paper focuses on localizing a set of UTs arbitrarily predeployed at unknown locations. Once the UT locations are known, they could serve as reference beacons for underwater navigation.

This paper considers the following problem. An autonomous surface vehicle (ASV) makes acoustic range measurements to estimate the positions (i.e., localize) several predeployed UTs that are rigidly attached to the sea floor. Where should the ASV place itself to use range measurements to optimally localize the UTs?

This problem has similarities to optimal sensor deployment, to which many optimization criteria have been developed [4]–[8]. Among the most common optimization criteria is the D-optimality criterion, namely maximization of the logarithm of the determinant of the Fisher information matrix [9]. The D-optimality criterion yields the maximum reduction in target location uncertainty as measured by the volume of the uncertainty ellipsoid [10], [11]. An alternative criterion to D-optimality was proposed in [12], referred to as maximum innovative logarithm-determinant (MILD), which seeks to maximize the volume of the innovation matrix. MILD was shown to be both computationally efficient and identical to the D-optimality criterion under linear Gaussian assumptions and was demonstrated to yield comparable performance with nonlinear pseudorange measurements. Another computationally efficient criterion with a geometric interpretation that approximately minimizes the dilution of precision was proposed in [13]. This criterion was shown to yield a family of convex programs that can be solved in parallel. A collaborative sensor placement strategy was developed in [14], wherein a network of coordinated ASVs attempt to optimally place themselves to localize a single UT. The dual of this problem, wherein landmarks are optimally placed to aid in vehicle positioning, was explored in [15].

While classical sensor placement problems consider planar environments, a three-dimensional (3-D) sensor placement strategy is needed for certain underwater and aerial applications. In underwater applications, an additional complexity arises from the fact that, once submerged, an autonomous underwater vehicle (AUV) is deprived of

GNSS signals; hence, GNSS-derived positioning<sup>1</sup> information becomes unavailable. This forces a reliance on onboard inertial sensor suites that provide positioning estimates that deteriorate over time in the absence of an aiding source (e.g., GNSS or signals of opportunity [16], [17]). Underwater simultaneous localization and mapping (SLAM) techniques have been developed to mitigate such deterioration [18].

Inertial sensors may be made robust to integral effects and drift via real-time corrections. This requires sensors (e.g., acoustic, magnetic, and pressure) to periodically correct for inertial navigation system (INS) drift [19]. The standard long baseline (LBL) acoustic approach to aided inertial navigation uses an extended Kalman filter to fuse ranges to multiple UTs with other AUV sensors [20]. An alternative approach to LBL was developed in [21], which uses an imaging sonar. Several magnetic/geomagnetic field-aided approaches have been developed. The inversion of the gradient of the magnetic field vector associated with a magnetic dipole at a fixed, known location was proposed in [22]. Simulated results emphasize the improvement in navigation quality (i.e., the decrease in vehicle position error) by utilizing tensor Euler deconvolution in tandem with eigenanalysis of the magnetic gradient tensor. This paper is motivated by the computational issues associated with analytical magnetic field inversion (i.e., when the magnetic field gradient tensor is singular). Another robust, computationally efficient algorithm for magnetic-aided navigation was developed in [23]. An adaptive unscented Kalman filter for magnetic navigation in a SLAM framework (e.g., the magnetic dipole's position is unknown) was formulated in [24].

Environmental features may also be used to mitigate decay of quality of position estimates associated with inertial navigation. For example, a sonar-based terrain-aided navigation (TAN) framework was developed in [25] to aid an AUV. This is paired with the work in [22] to develop a hybrid TAN-magnetic aided INS in [26]. This system was shown to yield lower AUV position error than either TAN or magnetic-aided navigation methods alone. An adaptive particle filter approach using sonar is developed in [27]. In [28], criteria were developed to ensure observability of the nonlinear system when ranging to a single acoustic beacon, while [29] and [30] derive such criteria when measuring pseudoranges to multiple terrestrial signal transmitters.

Multistep look-ahead (MSLA) planning, also known as model-predictive control or receding horizon control, has seen several applications in SLAM-type problems. This scheme is adopted in [31] for AUV fleet formation control. In [32], MSLA trajectory planning was numerically evaluated for its prospective benefit in a robotic SLAM environment. A similar numerical evaluation was presented in [29] in both radio SLAM and mapping-only

scenarios of several terrestrial transmitters using pseudorange measurements. A hybrid receding horizon path planner/model predictive AUV controller for dynamic navigation based on environmental information was developed in [33]. An adaptive path planning framework was developed in [34] to react to hazardous environments while maneuvering at high speed. A receding horizon planner for antisubmarine warfare AUV applications that is feasible in real time was presented in [35]. The controller is able to drive the AUV in such a way as to minimize the localization error of a mobile undersea target based on measurements from a bistatic sonar array.

A single-step look-ahead optimal measurement location planning (OMLP) strategy was developed in [36], which specifies the next optimal location at which the ASV should place itself to make acoustic range measurements to the UTs. This paper extends [36] and makes three contributions. First, a maximum *a posteriori* (MAP) framework is developed to localize UTs from noisy acoustic range measurements. Second, an MSLA OMLP strategy is developed that plans future D-optimal measurement locations by specifying the ASV's yaw rate. Third, simulation and experimental results are presented demonstrating the superiority of the MSLA OMLP strategy over the single-step look-ahead as well as random ASV motion.

The remainder of this paper is organized as follows. Section II describes the ASV's dynamics and observation model. Section III formulates the UT localization and MSLA OMLP problems for an arbitrary number of UTs in the environment. Section IV presents a MAP approach to solve 1) the UT localization problem and 2) a computationally efficient approach to solve the OMLP problem. Section V presents simulation results demonstrating both solutions. Section VI presents experimental results showing OMLP for one and two UTs with a localization accuracy of a few meters. Concluding remarks are given in Section VII.

## II. MODEL DESCRIPTION

The following nomenclature and conventions will be used throughout this paper unless stated otherwise. Vectors will be column and represented by lower-case, italicized, and bold characters (e.g.,  $\mathbf{x}$ ). Matrices will be represented by upper-case bold characters (e.g.,  $\mathbf{X}$ ).

The symbol  $n$  will denote a specific measurement epoch, while  $N$  denotes the total number of measurements made by the ASV. The symbol  $M$  denotes the total number of UTs in the environment, while  $m = 1, \dots, M$  serves to index each UT. The symbol  $k$  corresponds to the number of steps planned by the MSLA OMLP. When  $k = 0$ , the ASV randomly plans the next measurement location.

### A. Vehicle State and Model

Let  $\mathbf{p}_V(n) \in \mathbb{R}^3$  represent the 3-D position of the ASV. The velocity of the ASV at measurement epoch  $n$  is  $\mathbf{v}_V(n) \in \mathbb{R}^3$  and is represented in the vehicle's coordinate frame. The optimal next location from which the ASV should make a

<sup>1</sup>In this paper, the term "positioning" refers to the vehicle estimating its own states. The term "localization" will be used in reference to a vehicle estimating the states of some other entity.

measurement is  $\mathbf{p}_V^*(n+1)$ . This location is determined by solving an optimization problem that is constrained by a kinematic model with a maximum distance constraint.

To adopt an MSLA structure, the following model is assumed to propagate the ASV's position  $\mathbf{p}_V$  and yaw angle  $\phi_V$

$$\Sigma_V : \begin{cases} \mathbf{p}_V(n+1) = \mathbf{p}_V(n) + \mathbf{R}_z[\phi_V(n+1)]\mathbf{v}_V(n)T \\ \phi_V(n+1) = \phi_V(n) + \omega_V(n)T, \quad n = 1, \dots, N \end{cases} \quad (1)$$

where  $T$  is the sampling period,  $\omega_V$  is the yaw rate, and  $\mathbf{R}_z$  is a rotation matrix about the z-axis of the local frame by angle  $\phi_V$ , which has the form

$$\mathbf{R}_z[\phi_V(n)] = \begin{bmatrix} \cos(\phi_V(n)) & -\sin(\phi_V(n)) & 0 \\ \sin(\phi_V(n)) & \cos(\phi_V(n)) & 0 \\ 0 & 0 & 1 \end{bmatrix}. \quad (2)$$

The model in (1) assumes that  $T$  is sufficiently small such that  $\phi_V$  and  $\mathbf{v}_V$  over  $nT \leq t < (n+1)T$  are constant.

The ASV's state is defined as  $\mathbf{x}_V \triangleq [\mathbf{p}_V^T, \phi_V]^T \in \mathbb{R}^4$ .

### B. UT State and Model

It is assumed that  $M$  UTs exist in the environment at fixed, unknown positions. Let  $\mathbf{p}_T^m \in \mathbb{R}^3$  be the position of the  $m$ th UT, which propagates according to  $\mathbf{p}_T(n+1) = \mathbf{p}_T(n)$ ,  $n = 1, 2, \dots, N$ .

### C. Observation Model

The acoustic range observation made by the ASV at the  $n$ th measurement epoch is related to the  $m$ th UT's position by

$$\mathbf{z}^m(n) = r^m(n) + w(n), \quad (3)$$

where  $r^m(n) \triangleq \|\mathbf{p}_V(n) - \mathbf{p}_T^m\|_2$  is the true range between the ASV and UT and  $\|\cdot\|_2$  is the Euclidean norm, and  $w$  is the measurement noise, which is modeled as  $w(n) \sim \mathcal{N}(0, \sigma^2)$  and assumed to be temporally independent as well as independent and identically distributed across all  $N$  measurement epochs. The vector of  $N$  range measurements to the  $m$ th UT is denoted by

$$\mathbf{z}^m = \mathbf{r}^m + \mathbf{w}^m \in \mathbb{R}^N, \quad (4)$$

where  $\mathbf{r}^m \triangleq [r^m(1), \dots, r^m(N)]^T$  and  $\mathbf{w}^m \triangleq [w^m(1), \dots, w^m(N)]^T$ . The distribution of the measurement vector is  $\mathbf{z}^m \sim \mathcal{N}(\mathbf{r}^m, \mathbf{R})$ , where  $\mathbf{R} = \sigma^2 \mathbf{I}_{N \times N}$ .

## III. UT LOCALIZATION AND MSLA OMLP PROBLEM FORMULATION

This section formulates the UT localization and MSLA OMLP problems. The set of all ASV locations is denoted by  ${}^N\mathcal{P}_V$ . This set is constructed as

$${}^N\mathcal{P}_V = \{\mathbf{p}_V(1), \dots, \mathbf{p}_V(N)\}. \quad (5)$$

The ASV positions are assumed to be known (e.g., from GNSS measurements). The estimate of the location of the

$m$ th UT ( $\mathbf{p}_T^m$ ) based on  $N$  range measurements is denoted by  $\hat{\mathbf{p}}_T^m(N)$ . The range can be predicted as

$$\hat{r}^m(n) \triangleq \|\hat{\mathbf{p}}_T^m(N) - \mathbf{p}_V(n)\|_2. \quad (6)$$

The vector of estimated ranges is

$$\hat{\mathbf{r}}^m \triangleq [\hat{r}^m(1), \dots, \hat{r}^m(N)]^T \in \mathbb{R}^N. \quad (7)$$

The Jacobian vector  $\mathbf{h}^m(n) \triangleq \frac{\partial \hat{r}^m(n)}{\partial \mathbf{p}_T^m} |_{\hat{\mathbf{p}}_T^m(n)}$  is

$$\mathbf{h}^m(n) = \frac{[\hat{\mathbf{p}}_T^m(N) - \mathbf{p}_V(n)]^T}{\hat{r}^m(n)} \in \mathbb{R}^{1 \times 3}. \quad (8)$$

The vectors in (8) can be stacked to form the matrix

$$\mathbf{H}^m = [(\mathbf{h}^m(1))^T, \dots, (\mathbf{h}^m(N))^T]^T \in \mathbb{R}^{N \times 3}. \quad (9)$$

**PROBLEM 1 UT LOCALIZATION:** Given  $\mathbf{z}^m$  and  ${}^N\mathcal{P}_V$ , estimate  $\mathbf{p}_T^m$ .

**PROBLEM 2 MSLA OMLP:** Given the set of UT estimates using  $N$  range measurements  $\{\hat{\mathbf{p}}_T^m(N)\}_{m=1}^M$ , determine the next  $k$  values of the yaw rate  $[\omega_V(N), \dots, \omega_V(N+k-1)]$  that will drive the ASV to the locations  $\{\mathbf{p}_V(N+1), \dots, \mathbf{p}_V(N+k)\}$  in order to minimize the aggregate uncertainty of the set of future estimates  $\{\hat{\mathbf{p}}_T^m(N+k)\}_{m=1}^M$ , as measured by the logarithm of the determinant of the corresponding estimation error covariance.

## IV. UT LOCALIZATION AND MSLA OMLP SOLUTION

This section presents solutions to the UT localization and OMLP problems, which were formulated in Section III.

### A. Solution to the UT Localization Problem

To reduce the linearization error on UT localization, an iterative Gauss–Newton approach is adopted [37] along with a MAP estimation formulation. The iterative estimation algorithm is initialized with an estimate and corresponding covariance, denoted by  ${}_0\hat{\mathbf{p}}_T^m$  and  ${}_0\mathbf{P}_T^m$ , respectively, with the assumption  ${}_0\hat{\mathbf{p}}_T^m \sim \mathcal{N}(\mathbf{p}_T^m, {}_0\mathbf{P}_T^m)$ . In the case when one has little information about  $\mathbf{p}_T^m$ ,  ${}_0\mathbf{P}_T^m$  is set to be very large.

In what follows, the presubscript  $j$  denotes the iteration number. Specifically, the estimate of  $\mathbf{p}_T^m$  at the  $j$ th iteration using  $N$  measurements is  ${}_j\hat{\mathbf{p}}_T^m(N)$ . Estimated ranges and Jacobians at the  $j$ th iteration,  ${}_j\hat{r}^m(n)$  and  ${}_j\mathbf{h}^m(n)$ , are computed by substituting  ${}_j\hat{\mathbf{p}}_T^m(N)$  into (6) and (8). Similarly,  ${}_j\hat{\mathbf{r}}^m$  and  ${}_j\mathbf{H}^m$  are constructed by substituting  ${}_j\hat{r}^m(n)$  and  ${}_j\mathbf{h}^m(n)$ ,  $\forall n \leq N$ , into (7) and (9).

A MAP framework for UT localization is adopted [37], [38]. The basic optimization problem is

$$\hat{\mathbf{p}}_T^m(N) \triangleq \underset{\mathbf{p}_T^m}{\operatorname{argmax}} [p(\mathbf{z}^m | \mathbf{p}_T^m) p(\mathbf{p}_T^m)]. \quad (10)$$

Define the composite vectors

$$\mathbf{y} \triangleq [(\mathbf{z}^m)^T, ({}_0\hat{\mathbf{p}}_T^m)^T]^T \quad (11)$$

$$\mathbf{f}(\mathbf{p}_T^m) \triangleq [(\mathbf{r}^m)^T, (\mathbf{p}_T^m)^T]^T. \quad (12)$$

The covariance matrix for  $\mathbf{y}$  is

$$\mathbf{C} = \text{blkdiag}[\mathbf{R}, ({}_0\mathbf{P}_T^m)], \quad (13)$$

where  $\text{blkdiag}(\cdot)$  denotes a block-diagonal matrix. Maximizing the objective function of (10) is equivalent to minimizing

$$\mathcal{J}_{\text{MAP}}(\mathbf{p}_T^m) \triangleq \frac{1}{2} [\mathbf{y} - \mathbf{f}(\mathbf{p}_T^m)]^\top \mathbf{C}^{-1} [\mathbf{y} - \mathbf{f}(\mathbf{p}_T^m)]. \quad (14)$$

This allows the maximization problem in (10) to be rewritten as

$$\hat{\mathbf{p}}_T^m(N) \triangleq \underset{\mathbf{p}_T^m}{\text{argmin}} \quad \mathcal{J}_{\text{MAP}}(\mathbf{p}_T^m). \quad (15)$$

The MAP estimate of  $\mathbf{p}_T^m$  is computed by solving the batch nonlinear least-squares optimization problem in (15) iteratively according to the following steps. Start the iteration counter with  $j = 0$ . Let the  $j$ th estimate of  $\mathbf{p}_T^m$  be  ${}_j\hat{\mathbf{p}}_T^m$ . The estimated range vector is  ${}_j\hat{\mathbf{r}}^m = \mathbf{r}^m|_{\mathbf{p}_T^m = {}_j\hat{\mathbf{p}}_T^m}$ . The vector  $\mathbf{f}(\mathbf{p}_T^m)$  is linearized around  ${}_j\hat{\mathbf{p}}_T^m$  at each iteration, yielding

$$\mathbf{f}(\mathbf{p}_T^m) \approx \mathbf{f}({}_j\hat{\mathbf{p}}_T^m) + \mathbf{V}_j \delta \mathbf{p}_j, \quad (16)$$

where

$$\mathbf{V}_j \triangleq \begin{bmatrix} \mathbf{H}^m({}_j\hat{\mathbf{p}}_T^m) \\ \mathbf{I}_{3 \times 3} \end{bmatrix} \in \mathbb{R}^{(N+3) \times 3} \quad (17)$$

$$\delta \mathbf{p}_j \triangleq \mathbf{p}_T^m - {}_j\hat{\mathbf{p}}_T^m. \quad (18)$$

Define  $\delta \mathbf{y}_j \triangleq \mathbf{y} - \mathbf{f}({}_j\hat{\mathbf{p}}_T^m)$  to simplify notation. The MAP objective function in (15) can be re-expressed as

$$\mathcal{J}_{\text{MAP}}(\delta \mathbf{p}_j) = (\delta \mathbf{y}_j - \mathbf{V}_j \delta \mathbf{p}_j)^\top \mathbf{C}^{-1} (\delta \mathbf{y}_j - \mathbf{V}_j \delta \mathbf{p}_j). \quad (19)$$

The linearized objective function (19) is minimized when

$$\delta \mathbf{p}_j \equiv (\mathbf{V}_j^\top \mathbf{C}^{-1} \mathbf{V}_j)^{-1} \mathbf{V}_j^\top \mathbf{C}^{-1} \delta \mathbf{y}_j. \quad (20)$$

The estimate at the next iteration is

$${}_{j+1}\hat{\mathbf{p}}_T^m = {}_j\hat{\mathbf{p}}_T^m + \delta \mathbf{p}_j, \quad (21)$$

where  ${}_j\hat{\mathbf{p}}_T^m$  is the  $j$ th estimate of the position of the  $m$ th UT, and  $\delta \mathbf{p}_j$  is defined in (20). The iterations continue until  $\|{}_{j+1}\hat{\mathbf{p}}_T^m - {}_j\hat{\mathbf{p}}_T^m\|_2 \leq \delta_{\min}$ , or as long as  $j \leq J_{\max}$ , for user-defined  $J_{\max}$  and  $\delta_{\min}$ . After convergence, the covariance is

$${}^N\mathbf{P}_T^m \equiv (\mathbf{V}_j^\top \mathbf{C}^{-1} \mathbf{V}_j)^{-1}. \quad (22)$$

## B. Solution to the MSLA OMLP Problem

The D-optimality criterion [39, p. 387] is used to determine the future  $k$ -step trajectory  $\{\mathbf{p}_V(N+n)\}_{n=1}^k$  to maximize the information gain. For this section, the subscript  $N$  corresponds to the number of previous ASV locations. The symbol  $\mathbf{Y}_N^m \in \mathbb{R}^{3 \times 3}$  denotes the information matrix after  $N$  ASV measurements to the  $m$ th UT (i.e.,  $\mathbf{Y}_N^m = ({}^N\mathbf{P}_T^m)^{-1}$ ).

The single-step look-ahead (i.e.,  $k = 1$ ), commonly referred to as a greedy strategy, was formulated in [36] as

$$\begin{aligned} \mathbf{x}^* &= \underset{\mathbf{x}}{\text{argmax}} \quad \mathcal{J}(\mathbf{x}) \\ &\text{subject to} \quad g(\mathbf{x}) \leq d_{\max}, \end{aligned} \quad (23)$$

where

$$\mathcal{J}(\mathbf{x}) \triangleq \log \det [\mathbf{Y}_{N+1}(\mathbf{x})] \quad (24)$$

$$\mathbf{Y}_{N+1} \triangleq \text{blkdiag}[\mathbf{Y}_{N+1}^1, \dots, \mathbf{Y}_{N+1}^M] \quad (25)$$

$$g(\mathbf{x}) \triangleq \|\mathbf{x} - \mathbf{p}_V(N)\|_2 \quad (26)$$

$$\mathbf{x} \triangleq \mathbf{p}_V(N+1). \quad (27)$$

The distance constraint  $d_{\max}$  represents the maximum distance the ASV may travel between epochs  $N$  and  $N+1$ .

In what follows, the single-step OMLP is generalized to the MSLA OMLP. Define

$$\mathbf{D}_{N+k}^m(\omega_k) \triangleq (\mathbf{h}^m(N+k))^\top \mathbf{h}^m(N+k)$$

where the symbol  $\omega_k \triangleq \omega_V(N+k-1)$  is used to simplify notation. Recall from (8) that  $\mathbf{h}^m(N+k)$  depends on  $\omega_k$  because  $\omega_V(\cdot)$  is integrated through (1) to determine  ${}^{N+k}\mathcal{P}_V$ .

The information about transponder  $m$  at epoch  $N+k$  may be expressed as

$$\begin{aligned} \mathbf{Y}_{N+k}^m(\omega_k) &\triangleq \sigma^{-2} (\mathbf{H}_{N+k}^m)^\top \mathbf{H}_{N+k}^m \\ &= \sigma^{-2} [(\mathbf{H}_{N+k-1}^m)^\top \mathbf{H}_{N+k-1}^m + \mathbf{D}_{N+k}^m(\omega_k)] \\ &= \mathbf{Y}_{N+k-1}^m + \sigma^{-2} \mathbf{D}_{N+k}^m(\omega_k). \end{aligned} \quad (28)$$

The information  $\mathbf{Y}_{N+k}^m$  may be expressed as a function of  $\mathbf{Y}_N^m$  by recursively using (28)

$$\mathbf{Y}_{N+k}^m(\omega_V) = \mathbf{Y}_N^m + \sigma^{-2} \sum_{n=1}^k \mathbf{D}_{N+n}^m(\omega_n), \quad (29)$$

where  $\omega_V = \{\omega_n\}_{n=1}^k$ .

The MSLA D-optimality problem is

$$\begin{aligned} \omega_V^* &= \underset{\omega_V}{\text{argmax}} \quad \mathcal{J}(\omega_V) \\ &\text{subject to} \quad \Sigma_V \\ &\quad \{g(\omega_V(n)) \leq \omega_{\max}\}_{n=1}^k, \end{aligned} \quad (30)$$

where

$$\mathcal{J}(\omega_V) \triangleq \log \det [\mathbf{Y}_{N+k}(\omega_V)] \quad (31)$$

$$\mathbf{Y}_{N+k} \triangleq \text{blkdiag}[\mathbf{Y}_{N+k}^1, \dots, \mathbf{Y}_{N+k}^M] \quad (32)$$

$$g(\omega_V(n)) \triangleq |\omega_n|. \quad (33)$$

The distance constraint in (23) is subsumed into  $\mathbf{v}_V$  in (1). The angular rate constraint  $g(\omega_V(n))$  restricts each  $\omega_n$  to an envelope of  $\pm \omega_{\max}$ . Notice that  $\mathbf{Y}_{N+k}^m(\omega_V)$  is determined via linearization about estimate  ${}^N\hat{\mathbf{p}}_T^m$ . The first element of  $\omega_V^*$ , namely  $\omega_1^*$ , is applied to maneuver the ASV to obtain  $\mathbf{x}_V(N+1)$  [cf. (1)], while the remaining elements  $\omega_2^*, \dots, \omega_k^*$  are discarded. Note that these elements are discarded since at the next epoch, the ASV will receive new acoustic measurements which will be used to obtain a ‘‘refined’’ solution by solving the MSLA again (i.e., recede the planning horizon). Also note that while these elements are discarded, they impact the obtained optimal solution  $\omega_1^*$ , which is computed as part of the multistep vector  $\omega_V^*$ .

Next, the MSLA D-optimality problem (30) is simplified by exploiting the block-diagonal structure of  $\mathbf{Y}_{N+k}(\omega_V)$

to write

$$\begin{aligned} \boldsymbol{\omega}_V^* &= \underset{\boldsymbol{\omega}_V}{\operatorname{argmax}} \quad \log f(\boldsymbol{\omega}_V) \\ \text{subject to} \quad & \Sigma_V \\ & \{g(\boldsymbol{\omega}_V(n)) \leq \omega_{\max}\}_{n=1}^k \end{aligned} \quad (34)$$

where  $f(\boldsymbol{\omega}_V) = \prod_{m=1}^M \det[\mathbf{Y}_{N+k}^m(\boldsymbol{\omega}_V)]$ . Using the properties of the logarithm function

$$\log f(\boldsymbol{\omega}_V) = \sum_{m=1}^M \log \det [\mathbf{Y}_{N+k}^m(\boldsymbol{\omega}_V)]. \quad (35)$$

Further simplifications may be made if  $\sigma^{-2} \sum_{n=1}^k \mathbf{D}_{N+n}^m(x_n)$  is linearly separable, i.e., if

$$\mathbf{Y}_{N+k}^m(\boldsymbol{\omega}_V) = \mathbf{Y}_N^m + \mathbf{d}_1(\boldsymbol{\omega}_V) \mathbf{d}_2^T(\boldsymbol{\omega}_V),$$

where the vectors  $\mathbf{d}_i(\boldsymbol{\omega}_V) \in \mathbb{R}^{3 \times 1}$ ,  $i = 1, 2$ . While this decomposition may not hold in general, it is clear from the form of (29) that this is true when  $k = 1$ . In this case,  $\mathbf{d}_i(\boldsymbol{\omega}_V) = (\mathbf{h}^m(N+1))^T$ . When this decomposition holds, the matrix determinant properties developed in Appendix A, namely (59), could be applied to (35) to give

$$\begin{aligned} \det [\mathbf{Y}_{N+k}^m(\boldsymbol{\omega}_V)] &= \det [\mathbf{Y}_N^m] \\ & \det [1 + \mathbf{d}_2^T(\boldsymbol{\omega}_V) (\mathbf{Y}_N^m)^{-1} \mathbf{d}_1(\boldsymbol{\omega}_V)]. \end{aligned} \quad (36)$$

Define

$$\alpha^m(\boldsymbol{\omega}_V) \triangleq \mathbf{d}_2^T(\boldsymbol{\omega}_V) (\mathbf{Y}_N^m)^{-1} \mathbf{d}_1(\boldsymbol{\omega}_V), \quad (37)$$

which is a positive scalar. Using (36) and (37), the optimization function in (35) can be simplified to

$$\log f(\boldsymbol{\omega}_V) = \sum_{m=1}^M \log [1 + \alpha^m(\boldsymbol{\omega}_V)] \det [\mathbf{Y}_N^m]. \quad (38)$$

Properties of the logarithm function allow further simplification to

$$\log f(\boldsymbol{\omega}_V) = \sum_{m=1}^M \log [1 + \alpha^m(\boldsymbol{\omega}_V)] + \sum_{m=1}^M \log \det [\mathbf{Y}_N^m]. \quad (39)$$

The term  $\sum_{m=1}^M \log \det [\mathbf{Y}_N^m]$  is constant with respect to  $\boldsymbol{\omega}_V$ , so it can be dropped from the optimization function.

Letting  $\tilde{\mathcal{J}}(\boldsymbol{\omega}_V) \triangleq \sum_{m=1}^M \log [1 + \alpha^m(\boldsymbol{\omega}_V)]$ , the optimization problem of (34) can be written as

$$\begin{aligned} \boldsymbol{\omega}_V^* &= \underset{\boldsymbol{\omega}_V}{\operatorname{argmax}} \quad \tilde{\mathcal{J}}(\boldsymbol{\omega}_V) \\ \text{subject to} \quad & \Sigma_V \\ & \{g(\boldsymbol{\omega}_V(n)) \leq \omega_{\max}\}_{n=1}^k. \end{aligned} \quad (40)$$

Note that for  $M = 1$ , (40) is the same as

$$\begin{aligned} \boldsymbol{\omega}_V^* &= \underset{\boldsymbol{\omega}_V}{\operatorname{argmax}} \quad \tilde{\mathcal{J}}'(\boldsymbol{\omega}_V) \\ \text{subject to} \quad & \Sigma_V \\ & \{g(\boldsymbol{\omega}_V(n)) \leq \omega_{\max}\}_{n=1}^k \end{aligned} \quad (41)$$

where  $\tilde{\mathcal{J}}'(\boldsymbol{\omega}_V) \triangleq \alpha(\boldsymbol{\omega}_V)$ .

TABLE I  
ASV Locations Used in Monte Carlo Analysis

Symbol	Value, m
$\mathbf{p}_V(1)$	$[5, 5, 0]^T$
$\mathbf{p}_V(2)$	$[-5, 5, 0]^T$
$\mathbf{p}_V(3)$	$[-5, -5, 0]^T$
$\mathbf{p}_V(4)$	$[5, -5, 0]^T$

## V. SIMULATION RESULTS

This section presents simulation results for the UT localization and MSLA OMLP problems. The following quantitative metrics will be used in this section. Define the position error vector of the  $m$ th UT at the  $n$ th epoch as

$$\tilde{\mathbf{p}}_T^m(n) \triangleq \mathbf{p}_T^m - \hat{\mathbf{p}}_T^m(n) \in \mathbb{R}^3. \quad (42)$$

The augmented position error vector for all  $M$  UTs is

$$\tilde{\mathbf{p}}_T(n) \triangleq [(\tilde{\mathbf{p}}_T^1(n))^T, \dots, (\tilde{\mathbf{p}}_T^M(n))^T]^T \in \mathbb{R}^{3M}. \quad (43)$$

The magnitude of the position error vector is  $\|\tilde{\mathbf{p}}_T^m(n)\|_2$ . The normalized estimation error squared (NEES) at epoch  $n$  is

$$\epsilon(n) \triangleq \tilde{\mathbf{p}}_T^T(n) \mathbf{Y}_n \tilde{\mathbf{p}}_T(n). \quad (44)$$

The localization performance is evaluated using Monte Carlo tests. Let  $c \in \{1, 2, \dots, C\}$  be the index of a specific Monte Carlo trial. The localization root-mean-square estimation error (RMSEE) of the  $m$ th UT at the  $n$ th epoch is defined as

$$\bar{\mathbf{p}}_T^m(n) \triangleq \sqrt{\frac{1}{C} \sum_{c=1}^C \|\tilde{\mathbf{p}}_T^m(n)\|_2^2}. \quad (45)$$

The D-optimal value at the  $n$ th measurement epoch is denoted by  $\log \det [\mathbf{Y}_n]$ . The average computational time will be denoted by  $\bar{t}_c$ .

### A. Gauss–Newton MAP Estimator for UT Localization

The Gauss–Newton MAP estimator developed in Section IV-A assumes the measurement noise to be independent across different UT range measurements. Therefore, each UT may be estimated independently. This section evaluates the Gauss–Newton MAP estimator on a single UT for a prescribed ASV trajectory. The superscript  $m = 1$  is dropped in this section. A Monte Carlo analysis is performed, simulating 500 runs of the MAP estimation algorithm. For each run, the ASV made  $N = 4$  measurements from the locations listed in Table I to localize  $\mathbf{p}_T$ .

The UT was fixed at  $\mathbf{p}_T = [17, 15, -6]^T$ . The value  ${}_0\hat{\mathbf{p}}_T$  was drawn from a Gaussian distribution with covariance  ${}_0\mathbf{P}_T = \text{blkdiag}[100, 100, 4]$  and mean  $\mathbf{p}_T$ . The USBL measurement noise, defined in (4), has  $\sigma = 0.1$  m based on the SeaTrac x150 USBL product sheet [40].

The actual 95% confidence ellipse was calculated in the Easting–Northing (E–N) plane by substituting the

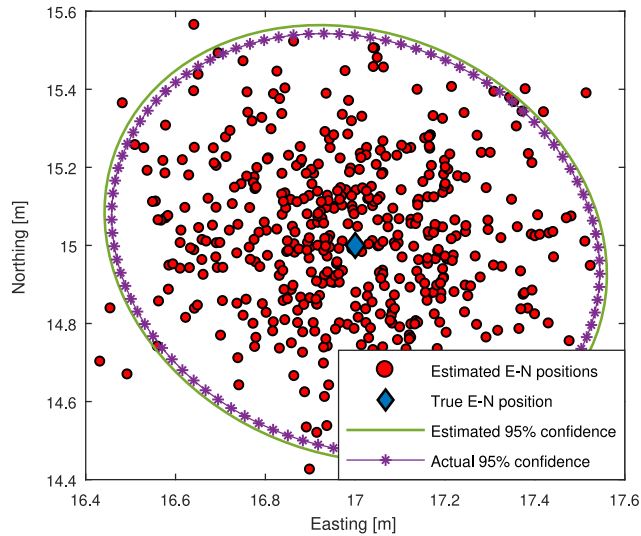


Fig. 1. Scatter plot of  $\hat{\mathbf{p}}_T(4)$  in the  $E - N$  plane.

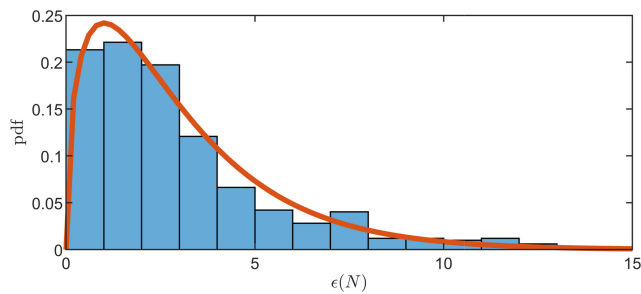


Fig. 2. Histogram of (44) at measurement epoch  $n = N = 4$  for all Monte Carlo runs. The orange curve displays a  $\chi_3^2$  pdf.

upper-left  $2 \times 2$  block of (22) and associated elements of (21) into the equations of Appendix B. Also, the estimated 95% confidence ellipse fitted to 500 samples of  $\hat{\mathbf{p}}_T(4)$  was calculated in the E-N plane using the equations in Appendix B. Fig. 1 compares these ellipses and shows them to be comparable.

The NEES of the MAP estimator will be evaluated next. It is expected that  $\epsilon(n) \sim \chi_{3M}^2$  (i.e., has a chi-squared probability density function (pdf) with  $3M$  degrees of freedom). Fig. 2 displays a normalized histogram of (44) at epoch  $n = N = 4$  across all Monte Carlo runs. A curve corresponding to a  $\chi_3^2$  distribution is overlaid onto this histogram. The curve fits the values of (44) closely, further validating that the estimator is performing correctly.

### B. MSLA OMLP Evaluation for $M = 1$

This section evaluates the MSLA OMLP for the single UT environment (the superscript  $m$  is dropped from this section). Again, a Monte Carlo analysis is performed. For this analysis, 1000 runs consisting of 50 (i.e.,  $N = 50$ ) acoustic measurements were simulated. Table II summarizes the simulation settings. The initial UT location  ${}_0\hat{\mathbf{p}}_T$  is drawn from a Gaussian distribution with mean  $\mathbf{p}_T$  and covariance  ${}_0\mathbf{P}_T = \text{blkdiag}[10^4, 10^4, 4]$  for all Monte Carlo runs. Three look-ahead lengths were simulated:  $k = 1, 2,$

TABLE II  
Single UT Localization Simulation Settings

Symbol	Value
$\mathbf{p}_V(1)$	$[-3, 9, 0]^T$ m
$\phi_V(1)$	$-30^\circ$
$\mathbf{p}_T$	$[17, 15, -6]^T$ m
$T$	1 s
$\mathbf{u}_V$	$[3, 0, 0]^T$ m/s
$\omega_{\max}$	$30^\circ/\text{s}$
$\sigma$	0.12 m

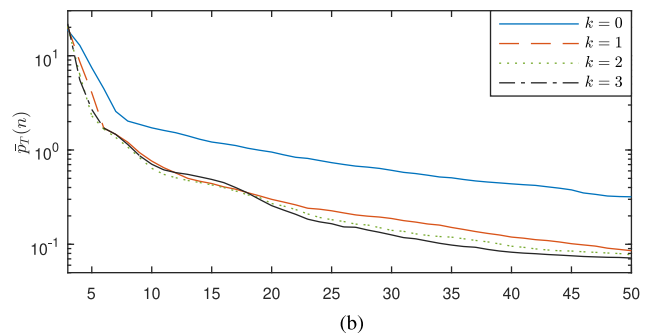
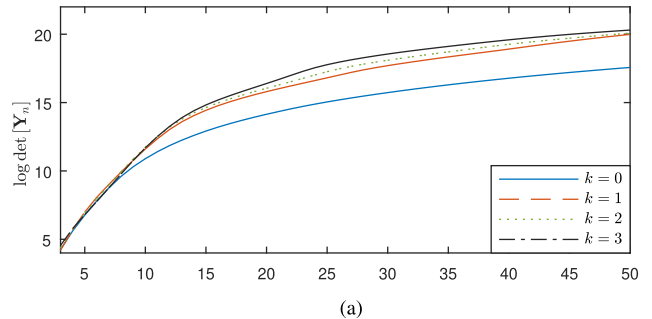


Fig. 3. Evolution of (a) D-optimal value and (b) localization RMSEE (45) as functions of measurement number  $n$ . These values are shown for various values of  $k$  ( $k = 0$  denotes a random ASV trajectory).

and 3. Additionally, a random ASV trajectory ( $k = 0$ ) was simulated, subject to the constraints in (34) to demonstrate the benefit gained from planning the measurement locations to improve UT localization.

It is expected that the D-optimal value obtained by using larger values of  $k$  will be larger than those obtained for smaller  $k$  at the cost of longer average computational time. However, due to the linearizations made in (29), there may be discrepancies in this trend at earlier measurement epochs. This trend in D-optimal value should in turn yield smaller values of (45). Additionally, it is intuitive to expect (45) and the D-optimal value to approach lower and upper bounds, respectively, determined by the number of measurements  $N$ , limiting the performance enhancements achievable by increasing  $k$ .

Fig. 3 displays the D-optimal value and (45) for various values of  $k$  as functions of  $n$ . These values are averaged over all Monte Carlo runs. Table III presents results for this simulation at specific epochs indicated by  $n$ . Rows of

TABLE III  
Single UT Localization Simulation Results

epoch	$k$	$\bar{p}_T(n)$ [m]	$\log \det [\mathbf{Y}_n]$	$\sigma_{\log \det} [\mathbf{Y}_n]$
$n = 3$	0	18.61	4.24	0.70
	1	20.06	4.22	0.94
	2	20.37	4.38	0.80
	3	21.55	4.55	0.51
$n = 7$	0	2.56	8.77	0.65
	1	1.46	9.02	0.87
	2	1.36	8.98	0.93
	3	1.46	8.77	0.84
$n = 30$	0	0.61	15.73	1.68
	1	0.19	17.70	1.34
	2	0.14	18.10	1.13
	3	0.13	18.55	0.95

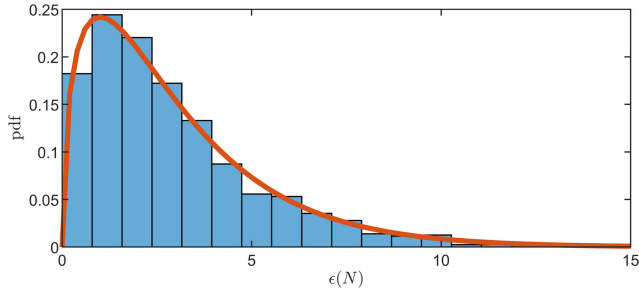


Fig. 4. Histogram of (44) at measurement epoch  $n = N = 50$  for all Monte Carlo runs in a single UT setup. The orange curve displays a  $\chi_3^2$  pdf.

this table organize data for different look-ahead duration indicated by  $k$ .

It is clear from Table III that the expected data trend holds in general. However, there are discrepancies in certain values at certain epochs. Nevertheless, these discrepancies are insignificant considering the magnitude of the standard deviation associated with these values at these epochs (the last column of Table III). The value  $\bar{t}_c$  (in seconds) increases from 0.18 s when  $k = 1$ , to 0.43 s when  $k = 2$ , to 0.88 s when  $k = 3$ .

It is worthwhile to verify the consistency of the estimator developed in Section IV-A when applied to the MSLA OMLP problem. The normalized position error (44) may be examined as in Section V-A. It is expected that (44) will be distributed according to a chi-squared pdf with  $3M = 3$  degrees of freedom. Fig. 4 presents the histogram of this value at measurement epoch  $n = N$  over all Monte Carlo runs for the  $k = 2$  planner. It is clear that (44) follows the expected distribution, suggesting the estimator is consistent. This trend was observed for the values of  $k = 1$  and  $k = 3$  as well.

It was empirically demonstrated in [36] that the solution to the greedy OMLP problem is achieved when  $\mathbf{h}(N + 1)$  is collinear with the eigenvector associated with the largest eigenvalue of  $\mathbf{Y}_N$ . This solution could be achieved by increasing the maximum allowable distance the ASV could move between measurements. In the new framework, however, this solution requires varying the ASV's forward

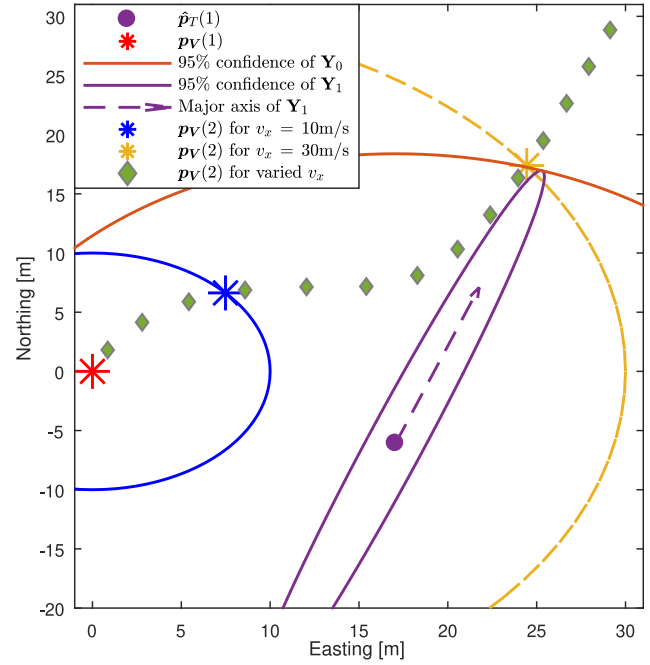


Fig. 5. Optimally planned ASV measurement locations determined at epoch  $n = 1$  for  $k = 1$ . The green sequence of diamonds indicates the optimal solution  $\mathbf{p}_V^*(2)$  as a function of  $v_x$ . The red asterisk denotes  $\mathbf{p}_V(1)$ . The eigenvector corresponding to the largest eigenvalue of  $\mathbf{Y}_1$  is denoted by the dashed purple arrow pointing in the direction of the major axis of the purple ellipse.

velocity, denoted by  $v_x$ , while fixing  $\omega_{\max} = \frac{180^\circ}{T}$ . This demonstration focuses on the planned ASV location after the first measurement has been made (i.e.,  $N = 1$ ). Fig. 5<sup>2</sup> displays the resulting  $\mathbf{p}_V^*(2)$  as  $v_x$  is varied from 1 to 80 m/s in increments of 1 m/s. To avoid clutter, this figure displays  $\mathbf{p}_V^*(2)$  determined using a subset of  $v_x \in [1, 80]$  m/s. It is clear that this result is consistent with that presented in [36].

### C. MSLA OMLP Evaluation for $M = 4$

This section evaluates the MSLA OMLP for a multi-UT environment with  $M = 4$ . A Monte Carlo analysis with 1000 runs is performed in an identical fashion to that in Section V-B with the simulation settings tabulated in Table IV.

Fig. 6 displays the D-optimal value and (45) for various values of  $k$  as functions of  $n$ . These values are averaged over all Monte Carlo runs. These values are shown for specific epochs in Table V. Columns of this table present (45) of UT  $m = 2$ , the D-optimal value, and standard deviation in D-optimal value. Rows of this table organize data for different look-ahead duration  $k$  at specific epochs.

Again, it can be seen that the expected localization trends hold in general. Discrepancies in the D-optimal value trend may again be ignored considering the magnitude of the standard deviation associated with these values at these

<sup>2</sup>Two optimal measuring locations  $\mathbf{p}_V^*(N + 1)$  exist. Fig. 5 focuses on those solutions that lie along the axis pointing northeast.

TABLE IV  
Multiple UT ( $M = 4$ ) Localization  
Simulation Settings

Symbol	Value
$\mathbf{p}_V(1)$	$[-3, 9, 0]^T$ m
$\phi_V(1)$	$-30^\circ$
$\mathbf{p}_T^1$	$[17, 15, -6]^T$ m
$\mathbf{p}_T^2$	$[-2, -1, -7]^T$ m
$\mathbf{p}_T^3$	$[5, 5, -10]^T$ m
$\mathbf{p}_T^4$	$[-9, 13, -8]^T$ m
$T$	1 s
$\mathbf{u}_V$	$[3, 0, 0]$ m/s
$\omega_{\max}$	$30^\circ/\text{s}$
$\sigma$	0.12 m

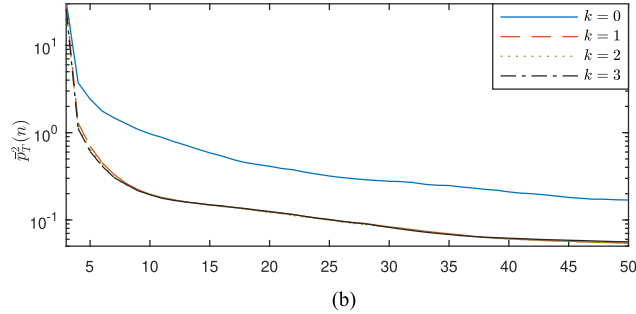
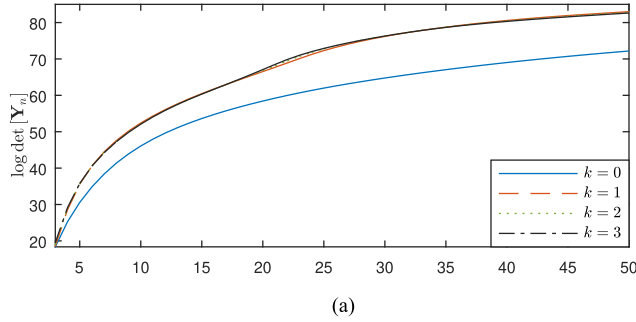


Fig. 6. Evolution of (a) D-optimal value and (b) localization RMSEE (45) as functions of measurement number  $n$  for the multiple UT environment. The D-optimal value is averaged over Monte Carlo runs. (b) Results for UT  $m = 2$ , as those for other UTs follow similar trends.

epochs (the last column in Table V). The average computational time  $\bar{t}_c$  increases from 0.24 s when  $k = 1$ , to 0.72 s when  $k = 2$ , to 1.62 s when  $k = 3$ .

As with the single UT case, the estimator is consistent when applied in an environment with multiple UTs. Fig. 7 presents the histogram of (44). It is clear that this histogram follows a  $\chi_{3M}^2$  distribution, indicating that the estimator is consistent.

Fig. 8 displays the measurement paths for each value of  $k$  during a single Monte Carlo run. The ASV's initial position was  $\mathbf{p}_V(1) = [-3, 9, 0]^T$  m with yaw angle  $\phi_V(1) = -30^\circ$ . Note that all optimally planned trajectories tend to orbit around the set of UTs. It is interesting to note the similarity between the trajectories planned using

TABLE V  
Multiple UT ( $M = 4$ ) Localization Simulation Results

epoch	$k$	$\bar{p}_T^m = 2(n)$ [m]	$\log \det [\mathbf{Y}_n]$	$\sigma_{\log \det [\mathbf{Y}_n]}$
$n = 3$	0	32.03	18.36	1.87
	1	28.82	18.59	3.19
	2	25.92	19.08	3.01
	3	26.05	19.54	2.77
$n = 7$	0	1.48	38.38	2.79
	1	0.33	44.47	0.67
	2	0.31	44.34	0.66
	3	0.13	44.23	0.63
$n = 30$	0	0.28	64.76	4.05
	1	0.08	76.19	0.54
	2	0.08	76.31	0.42
	3	0.08	76.30	0.33

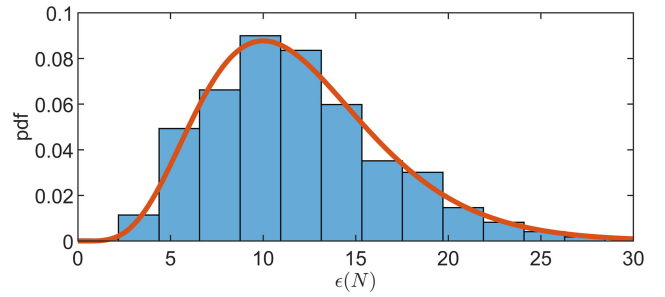


Fig. 7. Histogram of (44) at measurement epoch  $n = N = 50$  for all Monte Carlo runs in a multiple ( $M = 4$ ) UT setup. The orange curve displays a  $\chi_{12}^2$  pdf.

$k = 1$  and  $k = 2$ , and how they differ from that planned with  $k = 3$ . These trajectories begin to diverge at  $n = 30$ . From the data in Table V, it can be seen that both (45) and D-optimal value are very similar across all  $k \geq 1$  (i.e., for all optimally planned ASV trajectories) at this epoch.

## VI. EXPERIMENTAL RESULTS

This section presents experimental results for the UT localization and MSLA OMLP problems. The data collection scheme as well as analysis and description are provided. This section will use the same quantitative metrics of localization RMSEE (45) and D-optimal value.

### A. Data Collection

Data collection for both single and multiple transponder environments occurred on January 4, 2018 along pier 169 at SPAWAR SSC Pacific, San Diego, California, USA. Fig. 9 illustrates the testing environment. Two SeaTrac x010 acoustic beacons acted as UTs and were fixed to the pier at a depth of 1 m.

A manned surface craft equipped with a SeaTrac x150 USBL beacon and Hemisphere V104<sup>TM</sup> satellite-based augmentation system GPS Compass maneuvered in the ocean near the pier while ranging to each UT. The GPS re-

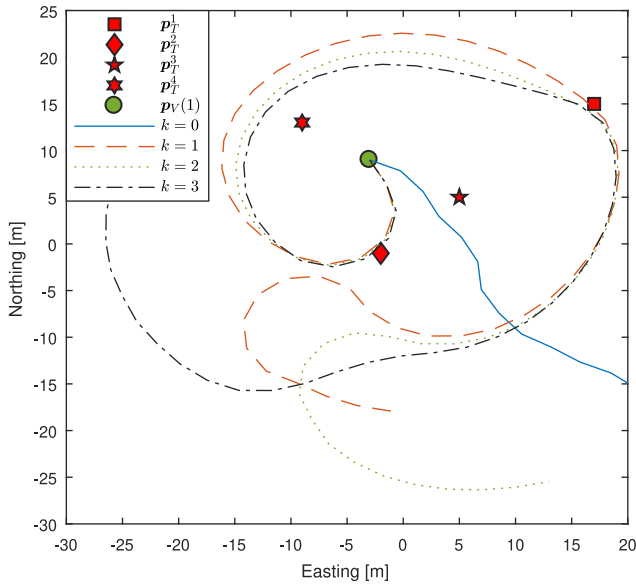


Fig. 8. Simulated ASV trajectories for various values of  $k$ . The initial ASV location is displayed as a green dot with a black outline.



Fig. 9. Top-down view of the testing area and acoustic ranging locations as measured by the Hemisphere V104™ GPS Compass. The orange dots are locations where USBL range measurements were made from the ASV to the UTs. The green push-pin markers display the configuration of UTs during data collection.

ceiver computed differential GPS (DGPS) position estimates, which were accurate to 1 m. Range data and GPS fixes were acquired at 0.67 Hz and 1 Hz, respectively, and were written to two separate files during data collection. All data was time-stamped with UTC time, which was used to align data in postprocessing. Ground truth positions of these UTs were determined by averaging GPS fixes at each UT mounting point over periods of 3 min.

## B. Noise Analysis

The range measurement standard deviation was estimated using sets of approximately 250 range measurements according to the procedure described in [36]. These values were estimated as  $\hat{\sigma}_1 = 62$  mm and  $\hat{\sigma}_2 = 113$  mm. For the

following, the maximum of both standard deviation estimates is used as the standard deviation associated with the USBL range sensor (i.e.,  $\sigma_{\text{USBL}} \equiv \max\{\hat{\sigma}_i\} = 113$  mm). It was also noted that  $\hat{r}_1$  is biased with respect to ground truth by approximately 0.2 m, which may be explained by the uncertainty associated with the GPS-derived estimates.

To compensate for these errors, one must first return to the models. First, let  $\hat{\mathbf{p}}_V(n)$  represent the estimate of the ASV location at measurement epoch  $n$  as determined via GPS. Additionally, evaluate the Jacobian vector  $\mathbf{h}^m(n)$  of (8) at the measurement location  $\hat{\mathbf{p}}_V(n)$

$$\mathbf{h}^m(n) = \frac{[\hat{\mathbf{p}}_T^m(N) - \hat{\mathbf{p}}_V(n)]^\top}{\hat{r}^m(n)} \in \mathbb{R}^{1 \times 3}. \quad (46)$$

Recall the model for the USBL range measurement in (3). The range can be approximated using a first-order Taylor series expansion around the current estimated UT location and ASV position at the  $n$ th measurement epoch (i.e.,  $\hat{\mathbf{p}}_T^m(N)$  and  $\hat{\mathbf{p}}_V(n)$ ). Define  $\check{r}^m(n)$  [cf. (6)] as

$$\check{r}^m(n) \triangleq \|\hat{\mathbf{p}}_T^m(N) - \hat{\mathbf{p}}_V(n)\|_2. \quad (47)$$

The approximated range is

$$z^m(n) \approx \check{r}^m(n) + \mathbf{h}^m(n) [\delta \mathbf{p}_T^m - \delta \mathbf{p}_V(n)] + w(n), \quad (48)$$

where

$$\delta \mathbf{p}_T^m \triangleq \hat{\mathbf{p}}_T^m(N) - \mathbf{p}_T^m(N) \quad (49)$$

$$\delta \mathbf{p}_V(n) \triangleq \hat{\mathbf{p}}_V(n) - \mathbf{p}_V(n). \quad (50)$$

The residual is defined as

$$\delta z^m(n) \triangleq z^m(n) - \check{r}^m(n) \quad (51)$$

$$= \mathbf{h}^m(n) \delta \mathbf{p}_T^m + w(n) - \mathbf{h}^m(n) \delta \mathbf{p}_V(n). \quad (52)$$

Define  $q(n) \triangleq \mathbf{h}^m(n) \delta \mathbf{p}_V(n)$  as the error due to uncertainty in the GPS solution. The total error in the range measurement is  $\epsilon(n) \triangleq w(n) + q(n)$ . It is reasonable to assume that  $w(n)$  and  $q(n)$  are white and are not correlated with each other.

With this in mind, the measurement noise may now be modeled as  $\epsilon(n) \sim \mathcal{N}(0, \sigma_\epsilon^2)$ , where  $\sigma_\epsilon^2 = \sigma_{\text{USBL}}^2 + \sigma_{\text{GPS}}^2$ . The value  $\sigma_{\text{GPS}}^2$  is the variance of  $q(n)$ . Note that, by construction of  $q(n)$ ,  $\sigma_{\text{GPS}}^2$  is the GPS position error projected onto  $\mathbf{h}^m(n)$ . For purposes of analysis,  $\sigma_{\text{GPS}}$  is set to be a constant (i.e.,  $\sigma_{\text{GPS}}^2 = 1$  m). With this assumption, the total measurement standard deviation is  $\sigma_\epsilon = 1.006$  m.

It is worth noting that in some practical applications, the noise covariance matrices may be poorly known and the “luxury” of characterizing them in this manner could be infeasible. To circumvent this issue, adaptive filters could be used [41].

## C. Processed Results: Evaluation of MSLA OMLP ( $M = 1$ )

This section evaluates the MSLA OMLP approach presented in Section IV-B for a single UT environment. All positions are represented in a local East, North, Up coordinate frame centered at the earliest collected GPS lo-

TABLE VI  
Single UT ( $M = 1$ ) Localization  
Experimental Settings

Symbol	Value
$\mathbf{p}_V(1)$	$[8.62, -6.77, 0]^T$ m
$\phi_V(1)$	$13^\circ$
$\mathbf{p}_T$	$[9.21, 1.68, -1.15]^T$ m
$T$	1 s
$\mathbf{u}_V$	$[3, 0, 0]$ m/s
$\omega_{\max}$	$30^\circ/\text{s}$
$\sigma_\epsilon$	1.006 m

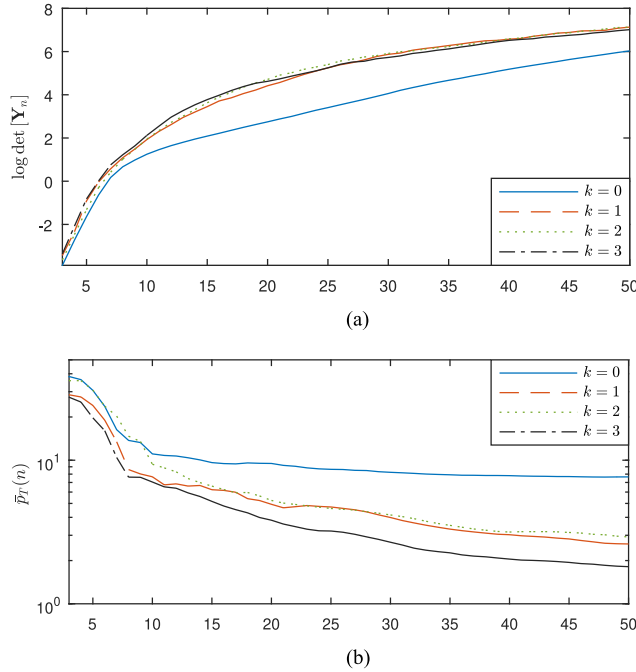


Fig. 10. Evolution of (a) D-optimal value and (b) localization RMSEE (45) as functions of measurement number  $n$  for the single UT experimental environment. These values are shown for various values of  $k$ .

cation of the ASV. This point, represented in the geodetic frame, is  ${}^g \mathbf{p}_V = [32.705^\circ \text{N}, 117.236^\circ \text{W}, -1.478 \text{ m}]$ . Again, a Monte Carlo analysis is performed. This analysis consists of 100 Monte Carlo runs. Each run has random initial estimates of transponder locations. An ASV trajectory comprising 50 measurement locations was produced for each run. The initial ASV position is held constant over all runs. Instead of simulating range measurements as was done in Section V-B, this section uses the range measurements collected at SPAWAR. The experimental settings are tabulated in Table VI.

Fig. 10 presents the D-optimal value and localization RMSEE (45). These values are averaged over all Monte Carlo runs. Localization results at specific epochs are given in Table VII. This table is organized identically to Table III. Note that, similar to the simulation analysis, one expects

TABLE VII  
Single UT Localization Experimental Results

epoch	$k$	$\bar{p}_T(n)$ [m]	$\log \det [\mathbf{Y}_n]$	$\sigma_{\log \det [\mathbf{Y}_n]}$
$n = 3$	0	38.28	-3.89	1.05
	1	28.55	-3.43	1.24
	2	35.78	-3.64	1.33
	3	27.46	-3.36	1.33
$n = 7$	0	16.32	0.17	0.84
	1	13.44	0.57	0.85
	2	20.29	0.42	1.21
	3	10.44	0.78	1.24
$n = 30$	0	8.23	4.08	1.06
	1	3.99	5.87	0.70
	2	4.15	5.91	0.74
	3	2.68	5.73	0.67

TABLE VIII  
Multiple UT ( $M = 2$ ) Localization  
Experimental Settings

Symbol	Value
$\mathbf{p}_V(1)$	$[8.62, -6.77, 0]^T$ m
$\phi_V(1)$	$13^\circ$
$\mathbf{p}_T^1$	$[9.21, 1.68, -1.15]^T$ m
$\mathbf{p}_T^2$	$[2.79, 0.44, -1.15]^T$ m
$T$	1 s
$\mathbf{u}_V$	$[3, 0, 0]$ m/s
$\omega_{\max}$	$30^\circ/\text{s}$
$\sigma_\epsilon$	1.006 m

that a larger value of  $k$  corresponds to better localization accuracy [i.e., smaller values of (45)]. This holds in general; however, discrepancies at all epochs for  $k = 2$  can be seen. Similarly, values of (45) are significantly larger than those observed in Section V-B. The most likely cause is that the GPS measurement of the UT position is not correct either due to GPS errors or the challenge of placing the GPS receiver directly above the UT. The average convergence time  $\bar{t}_c$  increases from 0.19 s when  $k = 1$ , to 0.39 s when  $k = 2$ , to 0.72 s when  $k = 3$ .

#### D. Processed Results: Evaluation of MSLA OMLP ( $M = 2$ )

This section evaluates the MSLA OMLP approach presented in Section IV-B for a multiple UT environment with  $M = 2$ . A Monte Carlo analysis is performed with the same setup as in Section VI-C. The experimental settings are tabulated in Table VIII. As with in the single UT case,  $\sigma_\epsilon = 1$  m.

Fig. 11 presents (45) and averaged D-optimal value as functions of measurement epoch. Values at selected epochs are provided in Table IX. As in previous cases, unexpected trends in the D-optimal value are insignificant considering the magnitude of the standard deviation associated with these values at these epochs. The values of (45) are larger than those in Section V-C. This increase is likely associated

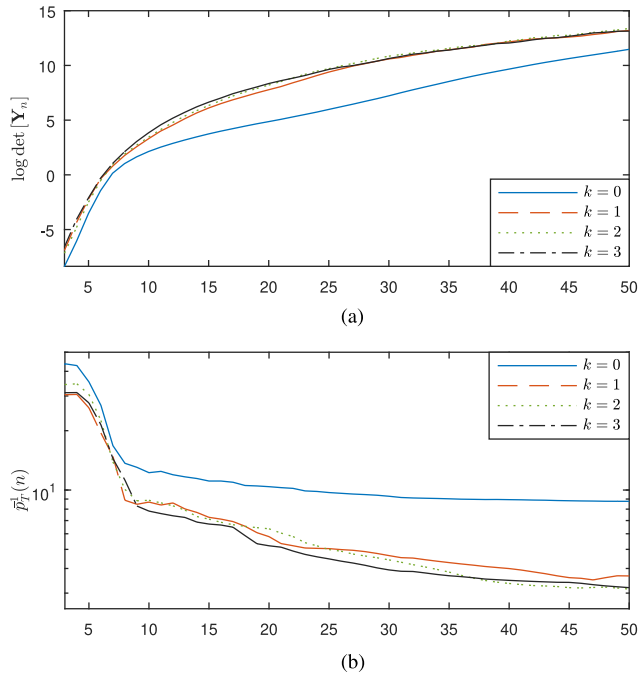


Fig. 11. Evolution of (a) averaged D-optimal value and (b) localization RMSEE (45) as functions of measurement number  $n$  for the multiple UT ( $M = 2$ ) experimental environment. These values are shown for various values of  $k$ . Note that (b) presents (45) for UT  $m = 1$  only, as that for UT  $m = 2$  is similar.

TABLE IX  
Multiple UT ( $M = 2$ ) Localization Experimental Results

epoch	$k$	$\bar{p}_T^{m=1}$ [m]	$\log \det [\mathbf{Y}_n]$	$\sigma_{\log \det} [\mathbf{Y}_n]$
$n = 3$	0	43.69	-8.36	1.72
	1	30.43	-6.90	2.06
	2	34.27	-7.16	2.14
	3	31.16	-6.58	2.07
$n = 7$	0	16.79	0.14	0.99
	1	14.81	0.79	1.28
	2	13.89	0.93	1.31
	3	14.43	1.03	1.58
$n = 30$	0	9.29	7.22	1.83
	1	4.65	10.59	1.73
	2	4.42	10.85	1.40
	3	3.93	10.63	1.25

with errors in the GPS measurement of the UT locations. The convergence time  $t_c$  increases from 0.21 s, to 0.48 s, to 0.99 s for the one-step, two-step, and three-step look-ahead planners, respectively.

Fig. 12 demonstrates the measurement paths determined by varying the value of  $k$ , along with the randomly planned trajectory, during a single Monte Carlo run.

The ASV's initial position is  $\mathbf{p}_V(1) = [8.62, -6.77, 0]^T$  m with yaw angle  $\phi_V(1) = 13^\circ$ . As in Section V-C, it can be seen that all optimally planned ASV trajectories orbit around the set of UTs.

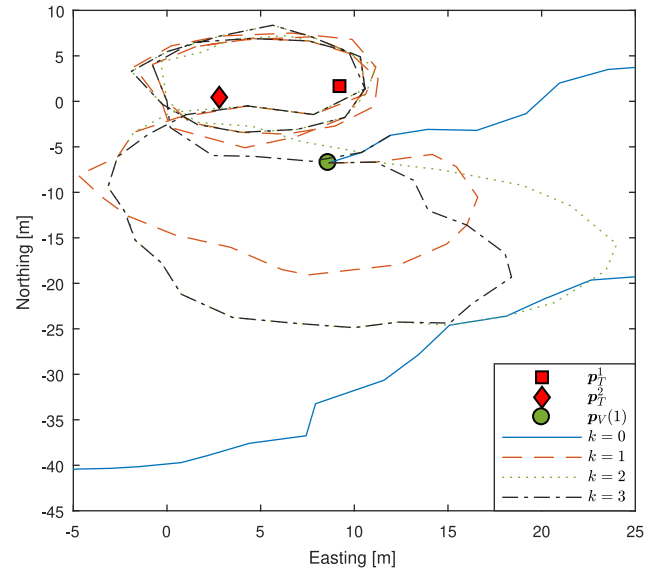


Fig. 12. ASV trajectories for various values of  $k$  using experimental data. UT locations are denoted by red symbols outlined in black. The initial ASV location is displayed as a green dot with a black outline.

## VII. CONCLUSION AND DISCUSSIONS

This paper provided a MAP estimation algorithm for localizing UTs as well as a strategy for the ASV to determine the best future locations at which acoustic ranges must be made to localize the UTs. The simulation results demonstrated the performance of the proposed MAP estimator and the OMLP strategy. The experimental results based on data collected at SPAWAR SSC Pacific demonstrated the performance of the MSLA OMLP strategy in an environment containing two UTs. Both simulation and experimental results demonstrated the localization benefit gained by the ASV when planning measurement locations as opposed to randomly choosing measurement locations. Additionally, localization accuracy is shown to increase for larger look-ahead distances at the cost of larger computational cost. It is interesting to note, however, that there are diminishing returns to larger look-ahead distances when considering longer measurement paths. In general, as the number of measurements increases, the marginal improvement in localization accuracy obtained from larger look-ahead distances is outweighed by the additional computational cost. Future research endeavors seek to adapt this problem to cases where an omnidirectional sensor may not be available. How might the use of a directional sensor change the planning method?

### APPENDIX A PROPERTIES OF MATRIX DETERMINANTS

Consider the block matrix  $\mathbf{Q} \in \mathbb{R}^{K \times K}$ , constructed as

$$\mathbf{Q} = \begin{bmatrix} \mathbf{A} & \mathbf{B} \\ \mathbf{C} & \mathbf{D} \end{bmatrix} \quad (53)$$

where  $\mathbf{A} \in \mathbb{R}^{M \times M}$ ,  $\mathbf{B} \in \mathbb{R}^{M \times N}$ ,  $\mathbf{C} \in \mathbb{R}^{N \times M}$ ,  $\mathbf{D} \in \mathbb{R}^{N \times N}$ , and  $N = K - M$ . When  $\mathbf{A}$  and  $\mathbf{D}$  are invertible

$$\det[\mathbf{Q}] = \det[\mathbf{A}] \det[\mathbf{D} - \mathbf{C}\mathbf{A}^{-1}\mathbf{B}] \quad (54)$$

$$= \det[\mathbf{D}] \det[\mathbf{A} - \mathbf{B}\mathbf{D}^{-1}\mathbf{C}]. \quad (55)$$

Now, consider the matrix  $\mathbf{Q}'$ , constructed as

$$\mathbf{Q}' = \begin{bmatrix} \mathbf{I} & \mathbf{B} \\ -\mathbf{C}^T & \mathbf{I} \end{bmatrix}. \quad (56)$$

Using (54) and (55)

$$\det[\mathbf{Q}'] = \det[\mathbf{I}] \det[\mathbf{I} + \mathbf{C}^T\mathbf{I}^{-1}\mathbf{B}] \quad (57)$$

$$= \det[\mathbf{I}] \det[\mathbf{I} + \mathbf{B}\mathbf{I}^{-1}\mathbf{C}^T]. \quad (58)$$

From (57) and (58), it is clear that

$$\det[\mathbf{I} + \mathbf{C}^T\mathbf{I}^{-1}\mathbf{B}] = \det[\mathbf{I} + \mathbf{B}\mathbf{I}^{-1}\mathbf{C}^T]. \quad (59)$$

## APPENDIX B

### CALCULATION OF CONFIDENCE ELLIPSES FROM CO-VARIANCE MATRICES

One may calculate the confidence ellipse corresponding to the estimate  $\hat{\mathbf{p}} \in \mathbb{R}^2$  and associated covariance matrix  $\mathbf{P} \in \mathbb{R}^{2 \times 2}$  as follows [42]. First, determine the largest eigenvalue and associated eigenvector (denoted  $\lambda_{\max}$  and  $\mathbf{v}_{\max} = [x_{\max}, y_{\max}]^T$ , respectively) of  $\mathbf{P}$ . Define the constants  $a \triangleq c\sqrt{\lambda_{\max}}$  and  $b \triangleq c\sqrt{\lambda_{\min}}$ , where  $c$  is a constant scaling factor corresponding to the desired confidence level of our ellipse. For a confidence level of 95%,  $c = 2.4477$ . Points along the confidence ellipse are now calculated as

$$\begin{bmatrix} x \\ y \end{bmatrix} = \hat{\mathbf{p}} + \mathbf{R}(\phi) \begin{bmatrix} a \cos(\theta) \\ b \sin(\theta) \end{bmatrix}, \quad \forall \theta \in [0, 2\pi), \quad (60)$$

where

$$\phi \triangleq \text{atan2}(y_{\max}, x_{\max}) \quad (61)$$

$$\mathbf{R}(\phi) \triangleq \begin{bmatrix} \cos(\phi) & -\sin(\phi) \\ \sin(\phi) & \cos(\phi) \end{bmatrix}. \quad (62)$$

## ACKNOWLEDGMENT

The authors would like to thank J. Khalife and E. Aghapour for helpful discussions and also the unmanned marine vehicles (UMV) lab and the members of HAMMER at SPAWAR SSC Pacific for help with data collection.

## REFERENCES

- [1] L. Paull, S. Saeedi, M. Seto, and H. Li  
AUV navigation and localization: A review  
*IEEE J. Ocean. Eng.*, vol. 39, no. 1, pp. 131–149, Jan. 2014.
- [2] S. Kim, B. Ku, W. Hong, and H. Ko  
Performance comparison of target localization for active sonar systems  
*IEEE Trans. Aerosp. Electron. Syst.*, vol. 44, no. 4, pp. 1371–1380, Oct. 2008.
- [3] Y. Huang, Y. Zhang, B. Xu, Z. Wu, and J. Chambers  
A new adaptive extended Kalman filter for cooperative localization  
*IEEE Trans. Aerosp. Electron. Syst.*, vol. 54, no. 1, pp. 353–368, Feb. 2018.
- [4] P. Zhan, D. Casbeer, and A. Swindlehurst  
Adaptive mobile sensor positioning for multi-static target tracking  
*IEEE Trans. Aerosp. Electron. Syst.*, vol. 46, no. 1, pp. 120–132, Jan. 2010.
- [5] J. Morales and Z. Kassas  
Optimal receiver placement for collaborative mapping of signals of opportunity  
In *Proc. ION GNSS Conf.*, Sep. 2015, pp. 2362–2368.
- [6] D. Moreno-Salinas, A. Pascoal, and J. Aranda  
Optimal sensor placement for acoustic underwater target positioning with range-only measurements  
*IEEE J. Ocean. Eng.*, vol. 41, no. 3, pp. 620–643, Jul. 2016.
- [7] X. Fang, W. Yan, and W. Chen  
Sensor placement for underwater source localization with fixed distances  
*IEEE Geosci. Remote Sens. Lett.*, vol. 13, no. 9, pp. 1379–1383, Sep. 2016.
- [8] J. Khalife and Z. Kassas  
Optimal sensor placement for dilution of precision minimization via quadratically constrained fractional programming  
*IEEE Trans. Aerosp. Electron. Syst.*, to be published.
- [9] D. Uciński  
*Optimal Meas. Methods for Distributed Parameter System Identification*. Boca Raton, FL, USA: CRC Press, 2005.
- [10] D. Moreno-Salinas, N. Crasta, M. Ribiero, B. Bayat, A. Pascoal, and J. Aranda  
Integrated motion planning, control, and estimation for range-based marine vehicle positioning and target localization  
In *Proc. IFAC Conf. Control Appl. Marine Syst.*, Sep. 2016, vol. 49, no. 23, pp. 34–40.
- [11] Z. Kassas and T. Humphreys  
Motion planning for optimal information gathering in opportunistic navigation systems  
In *Proc. AIAA Guid., Navig., Control Conf.*, Aug. 2013, pp. 4551–4565.
- [12] Z. Kassas, T. Humphreys, and A. Arapostathis  
Greedy motion planning for simultaneous signal landscape mapping and receiver localization  
*IEEE J. Sel. Topics Signal Process.*, vol. 9, no. 2, pp. 246–258, Mar. 2015.
- [13] J. Morales and Z. Kassas  
Optimal collaborative mapping of terrestrial transmitters: Receiver placement and performance characterization  
*IEEE Trans. Aerosp. Electron. Syst.*, vol. 54, no. 2, pp. 992–1007, Apr. 2018.
- [14] B. Ferriera, A. Matos, H. Campos, and N. Cruz  
Localization of a sound source: Optimal positioning of sensors carried on autonomous surface vehicles  
In *Proc. IEEE OCEANS Conf.*, Sep. 2013, pp. 1–8.
- [15] J. Perez-Ramirez, D. Borah, and D. Voelz  
Optimal 3-D landmark placement for vehicle localization using heterogeneous sensors  
*IEEE Trans. Veh. Technol.*, vol. 62, no. 7, pp. 2987–2999, Sep. 2013.
- [16] J. Morales, P. Roysdon, and Z. Kassas  
Signals of opportunity aided inertial navigation  
In *Proc. ION GNSS Conf.*, Sep. 2016, pp. 1492–1501.
- [17] J. Morales, J. Khalife, and Z. Kassas  
Collaborative autonomous vehicles with signals of opportunity aided inertial navigation systems  
In *Proc. ION Int. Tech. Meet. Conf.*, Jan. 2017, 805–818.

- [18] F. Hidalgo and T. Brunl  
Review of underwater SLAM techniques  
In *Proc. Int. Conf. Autom., Robot. Appl.*, Feb. 2015, pp. 306–311.
- [19] P. Miller, J. Farrell, Y. Zhao, and V. Djapic  
Autonomous underwater vehicle navigation  
*IEEE J. Ocean. Eng.*, vol. 35, no. 3, pp. 663–678, Jul. 2010.
- [20] J. Zhang, C. Shi, K. Tang, and Y. Han  
Research and implementation on multi-beacon aided AUV integrated navigation algorithm  
In *Proc. IEEE OCEANS Conf.*, Jun. 2017, pp. 1–5.
- [21] V. Djapic *et al.*  
Novel method for underwater navigation aiding using a companion underwater robot as a guiding platforms  
In *Proc. IEEE OCEANS Conf.*, Jun. 2013, pp. 1–10.
- [22] F. Teixeira and A. Pascoal  
Magnetic navigation and tracking of underwater vehicles  
*IFAC Proc. Volumes*, vol. 46, no. 33, pp. 239–244, 2013.
- [23] M. Ejaz, J. Iqbal, N. Ahsan, and A. Nawaz  
Robust geomagnetic aided inertial navigation of underwater vehicles using the ICP algorithm  
In *Proc. Asia Pac. Conf. Comput. Intell. Ind. Appl.*, Nov. 2009, vol. 1, pp. 257–262.
- [24] M. Wu and J. Yao  
Adaptive UKF-SLAM based on magnetic gradient inversion method for underwater navigation  
In *Proc. Int. Conf. Unmanned Aircraft Syst.*, Jun. 2015, pp. 839–843.
- [25] F. Teixeira, J. Quintas, and A. Pascoal  
AUV terrain-aided Doppler navigation using complementary filtering  
In *Proc. IFAC Conf. Maneuvering Control Marine Craft*, Sep. 2012, vol. 45, pp. 313–318.
- [26] J. Quintas, F. Teixeira, and A. Pascoal  
Magnetic signal processing methods with application to geophysical navigation of marine robotic vehicles  
In *Proc. IEEE OCEANS Conf.*, Sep. 2016, pp. 1–8.
- [27] T. Zhou, D. Peng, C. Xu, W. Zhang, and J. Shen  
Adaptive particle filter based on Kullback-Leibler distance for underwater terrain aided navigation with multi-beam sonar  
*IET Radar, Sonar Navigat.*, vol. 12, no. 4, pp. 433–441, 2018.
- [28] P. Batista, C. Silvestre, and P. Oliveira  
Single range aided navigation and source localization: Observability and filter design  
*Syst. Control Lett.*, vol. 60, no. 8, pp. 665–673, Jun. 2011.
- [29] Z. Kassas and T. Humphreys  
Receding horizon trajectory optimization in opportunistic navigation environments  
*IEEE Trans. Aerosp. Electron. Syst.*, vol. 51, no. 2, pp. 866–877, Apr. 2015.
- [30] Z. Kassas and T. Humphreys  
Observability analysis of collaborative opportunistic navigation with pseudorange measurements  
*IEEE Trans. Intell. Transp. Syst.*, vol. 15, no. 1, pp. 260–273, Feb. 2014.
- [31] H. Li, P. Xie, and W. Yan  
Receding horizon formation tracking control of constrained underactuated autonomous underwater vehicles  
*IEEE Trans. Ind. Electron.*, vol. 64, no. 6, pp. 5004–5013, Jun. 2017.
- [32] S. Huang, N. Kwok, G. Dissanayake, Q. Ha, and G. Fang  
Multi-step look-ahead trajectory planning in SLAM: Possibility and necessity  
In *Proc. IEEE Int. Conf. Robot. Autom.*, Apr. 2005, pp. 1091–1096.
- [33] C. Shen, Y. Shi, and B. Buckham  
Integrated path planning and tracking control of an AUV: A unified receding horizon optimization approach  
*IEEE/ASME Trans. Mechatron.*, vol. 22, no. 3, pp. 1163–1173, Jun. 2017.
- [34] M. Dunbabin and R. Lament  
Adaptive receding horizon control for a high-speed autonomous surface vehicle in narrow waterways  
In *Proc. IEEE Conf. Control Technol. Appl.*, Aug. 2017, pp. 235–240.
- [35] G. Ferri, A. Munafó, R. Goldhahn, and K. LePage  
A non-myopic, receding horizon control strategy for an AUV to track an underwater target in a bistatic sonar scenario  
In *Proc. IEEE Conf. Decis. Control*, Dec. 2014, pp. 5352–5358.
- [36] J. Garcia, J. Farrell, and Z. Kassas  
Optimal measurement location planning for localizing underwater transponders  
In *Proc. IEEE/ION Position Location Navigat. Symp.*, Apr. 2018, pp. 480–486.
- [37] Y. Bar-Shalom, T. Kirubarajan, and X. Li  
*Estimation with Applications to Tracking and Navigation*. Hoboken, NJ, USA: Wiley, 2002.
- [38] S. Kay  
*Fundamentals of Statistical Signal Processing: Estimation Theory*. Englewood Cliffs, NJ, USA: Prentice-Hall, 1993.
- [39] S. Boyd and L. Vandenberghe  
*Convex Optimization*. Cambridge, U.K.: Cambridge Univ. Press, 2004.
- [40] *SeaTrac Micro-USBL Tracking and Data Modems*, rev. 5, Blueprint Design Engineering Ltd, Mar. 2016. [Online]. Available: <https://www.blueprintsubsea.com/seatrac/support.php>
- [41] Y. Huang, Y. Zhang, B. Xu, Z. Wu, and J. A. Chambers  
A new adaptive extended Kalman filter for cooperative localization  
*IEEE Trans. Aerosp. Electron. Syst.*, vol. 54, no. 1, pp. 353–368, Feb. 2018.
- [42] W. Hoover and M. Rockville  
Algorithms for confidence circles and ellipses  
U.S. Dept. Commerce, Nat. Oceanic Atmospheric Admin., Washington, DC, USA, Tech. Rep. National Ocean Service (NOS) 107 Coast & Geodetic Survey (CGS) 3, Sep. 1984.



**Jesse R. Garcia** (S'16) received the B.S.(Hons.) degree in electrical and computer engineering from the University of California, Riverside, Riverside, CA, USA, in 2016, where he is currently working toward the M.S. degree in electrical engineering.

He is a member of the Autonomous Systems Perception, Intelligence, and Navigation (ASPIN) Laboratory. His research interests include underwater robotics, estimation, autonomous vehicles, and navigation.



**Jay A. Farrell** (F'08) received the B.S. degree in physics and electrical engineering from Iowa State University, Ames, IA, USA, in 1986, and the M.S. and Ph.D. degrees in electrical engineering from the University of Notre Dame, Notre Dame, IN, USA, in 1998 and 1989, respectively.

He is currently a Professor with the Department of Electrical and Computer Engineering, University of California, Riverside, where he has served three terms as Department Chair and is currently a Associate Dean. He has authored more than 250 technical publications and three books.

Dr. Farrell was the recipient of the Engineering Vice President's Best Technical Publication Award at Charles Stark Draper Lab (1989–1994) in 1990, and Recognition Awards for Outstanding Performance and Achievement in 1991 and 1993. He was named a GNSS Leader to Watch for 2009–2010 by GPS World Magazine and a winner of the Connected Vehicle Technology Challenge by the U.S. Department of Transportation's (DOT's) Research and Innovative Technology Administration in July 2011. He is a Fellow of AAAS, a Distinguished Member of IEEE CSS. He was the IEEE Control Systems Society as General Chair of IEEE CDC 2012, and as President in 2014. He is currently an American Automatic Control Council Vice President in 2018.



**Zaher M. Kassas** (S'98–M'08–SM'11) received the B.E.(Hons.) degree in electrical engineering from the Lebanese American University, Beirut, Lebanon, in 2001, the M.S. degree in electrical and computer engineering from The Ohio State University, Columbus, OH, USA, in 2003, and the M.S.E. degree in aerospace engineering and the Ph.D. degree in electrical and computer engineering from The University of Texas at Austin, Austin, TX, USA, in 2010 and 2014, respectively.

He is currently an Assistant Professor with the University of California, Riverside, Riverside, Ca, USA, and the Director of the Autonomous Systems Perception, Intelligence, and Navigation (ASPIN) Laboratory. His research interests include cyber-physical systems, estimation theory, navigation systems, autonomous vehicles, and intelligent transportation systems.

Dr. Kassas was the recipient of the National Science Foundation (NSF) Faculty Early Career Development Program (CAREER) award in 2018, the Office of Naval Research (ONR) Young Investigator Program (YIP) award in 2019, and the 2018 IEEE Walter Fried Award and the 2018 ION Samuel Burka Award.



**Michael T. Ouimet** received the B.S degree in mechanical engineering from the University of Notre Dame, Notre Dame, IN, USA, and the M.S. and Ph.D. degrees in mechanical and aerospace engineering from University of California, San Diego, La Jolla, CA, USA.

He is currently with the Unmanned Maritime Vehicles lab, SSC Pacific as a Researcher. His main research interests include autonomy for multiagent unmanned systems, especially in the intersection of control theory, artificial intelligence, and machine learning for robotics.